Validation of Vertical Mixing in an Equatorial Ocean Model Using Large Eddy Simulations and Observations

WILLIAM G. LARGE AND PETER R. GENT

National Center for Atmospheric Research, Boulder, Colorado

(Manuscript received 24 October 1997, in final form 26 March 1998)

ABSTRACT

A nonlocal K-profile parameterization (KPP) of the upper-ocean boundary layer is tested for the equatorial regions. First, the short-term performance of a one-dimensional model with KPP is found to compare favorably to large eddy simulations (LES), including nonlocal countergradient heat flux. The comparison is clean because both the surface forcing and the large-scale flow are identical in the two models. The comparison is direct because the parameterized turbulent flux profiles are explicitly computed in LES. A similar comparison is less favorable when KPP is replaced by purely downgradient diffusion with Richardson-number-dependent viscosity and diffusivity because of the absence of intense convection after sunset. Sensitivity experiments are used to establish parameter values in the interior mixing of KPP.

Second, the impact of the parameterization on annual means and the seasonal cycle in a general circulation model of the upper, equatorial Pacific Ocean is described. The results of GCM runs with and without KPP are compared to annual mean profiles of zonal velocity and temperature from the TOGA-TAO array. The two GCM solutions are closer to each other than to the observations, with biases in zonal velocity in the western Pacific and in subsurface temperature in the eastern Pacific. Such comparisons are never clean because neither the wind stress and the surface heat flux nor the forcing by the large-scale flow are known to sufficient accuracy.

Finally, comparisons are made of the equatorial Pacific Ocean GCM results when different heat flux formulations are used. These include bulk forcing where prescribed air temperature and humidity are used, SST forcing where the use of such ocean-controlled parameters is avoided, and a fully coupled atmospheric general circulation model where there is no prescribed control over any surface fluxes. It is concluded, especially in the eastern Pacific, that the use of specified air temperature and humidity does not overly constrain the model sea surface temperature.

1. Introduction

The equatorial ocean is a unique region where vertical mixing is of primary importance. Dynamically, the dominance of geostrophic balance diminishes toward the equator, and near the surface the zonal pressure gradient becomes balanced by wind-stress-induced vertical mixing. Deeper this pressure gradient is only partially balanced by a baroclinic pressure gradient, vertical advection, and horizontal processes. The remaining imbalance accelerates the Equatorial Undercurrent (EUC) to the point where vertical mixing near its core makes up the difference. These balances and dynamic adjustments, including equatorial waves, are discussed in detail by Gill (1982). Thermodynamically, the dominant near-surface balance is between solar heating and vertical advection (upwelling) of cold deeper water, but perturbations of this balance are largely due to vertical mixing. Philander (1990) asserts that vertical mixing processes affect the intensity of equatorial currents and are necessary for the upwelling to produce the distinctive patterns of observed sea surface temperature (SST).

Vertical mixing occurs at the smaller scales (order 0.1–10 m) of oceanic motion. Therefore, it is not easily observed, nor modeled. In most ocean models computational considerations dictate that it be parameterized. For vertical mixing at the equator, Pacanowski and Philander (1981) proposed a scheme based on the local gradient Richardson number. This parameterization was needed in the high vertical shear zone of the equatorial undercurrent, and was quite successful, and is still used in many tropical ocean simulations. Chen et al. (1994a) recently developed a vertical mixing parameterization based on a Kraus–Turner (1967) type mixed layer model and the Price et al. (1986) dynamical instability model. This hybrid scheme has been tested in tropical ocean models and Chen et al. (1994b) show how it improves the simulation of the annual cycle of SST in the eastern Pacific Ocean.

Large eddy simulation (LES) represents a different class of ocean model, where the domain is made arti-

Corresponding author address: Dr. William G. Large, National Center for Atmospheric Research, 1850 Table Mesa Drive, P.O. Box 3000, Boulder, CO 80303.
E-mail: wily@ncar.ucar.edu

ficially small (order 100 m) to allow sufficient resolution (order 1 m) to resolve explicitly the most energetic turbulent eddies. Thus, subgrid-scale parameterizations contribute little to mixing over most of the domain and so have relatively little effect on LES solutions. This technique was pioneered by Deardorff (1970, 1972) for numerical investigations of laboratory and atmospheric convection. It has been successfully applied to many atmospheric studies (e.g., Wyngaard and Brost 1984; Moeng and Wyngaard 1984), including evaluations of boundary-layer turbulence closures (Moeng and Wyngaard 1989; Ayotte et al. 1996).

Recently, LES models have been applied to ocean problems (e.g., Skyllingstad and Denbo 1995; McWilliams et al. 1997), including turbulent mixing in the upper-equatorial ocean (Wang et al. 1996, 1998; Skyllingstad et al. 1999). These equatorial studies addressed the diurnal cycle of solar heating, the horizontal component of the earth's rotation, eddy viscosity, the diurnal cycle of deep turbulence, and turbulent dissipation during a westerly wind burst. Since the precise forcing, initial conditions, and physics of these LES solutions are known, their solutions are ideal datasets for evaluating the short-term (several days) performance of one-dimensional ocean models and their parameterized vertical mixing.

In contrast to LES, ocean models designed for climate research place severe demands on vertical mixing parameterizations. They must capture the important physics throughout the annual cycle in very different dynamical regimes, including the equatorial ocean, without computational demands that would preclude the long climate integration times. In response to this challenge, Large et al. (1994) developed a nonlocal K-profile parameterization (KPP) of vertical mixing throughout the water column. They used midlatitude observational datasets to choose parameter values and to verify one-dimensional model performance over timescales from hours to years. However, they made no attempt to simulate equatorial ocean behavior because a means of verification was lacking. Two major problems with using equatorial ocean observations for this purpose are inaccuracies in the observed forcing and unknown effects of the full three-dimensional flow. Neither of these problems are present in LES data.

The outstanding issue of KPP validation at the equator needs to be addressed, and this is the primary purpose of the present study. First, the short-term performance will be compared with the LES results of Wang et al. (1998). Second, the impact on annual means and the seasonal SST cycle of the equatorial Pacific model of Gent and Cane (1989) will be assessed. Chen et al. (1994a) attribute several improvements in the same Pacific model to their hybrid scheme. Similar impacts are expected with the KPP scheme because it contains all the physics of the hybrid model, namely rapid mixing in the mixed layer and smaller, but significant, shear driven mixing below. In addition, KPP physics includes nonlocal turbulent transfer, finite as opposed to infinite mixing rates in the mixed layer, as well as penetrative wind and buoyancy driven convection. However, apparent improvements relative to observations also depend on the surface forcing and other model physics.

The sensitivity of equatorial SST to the surface forcing has been demonstrated by Chen et al. (1994b) and will not be repeated here. However, Seager et al. (1988) raise the issue of heat flux formulations and argue for what we will term ''SST'' forcing where the heat flux only depends on model SST and on specified wind speed and cloud cover. Their concern is that, if specified atmospheric parameters such as air temperature and humidity, which are directly controlled by the ocean, are used in the heat flux formulation, then the SST is to a large extent also specified. Such ''bulk'' forcing is employed globally by Large et al. (1997) with some success and will be used here too (section 4). In addition, the Gent and Cane ocean model will be SST forced and will be fully coupled to an atmospheric general circulation model (section 5). In the latter case the heat flux formulation is not an issue.

2. The K-profile parameterization

Let x represent a general prognostic model variable such as zonal velocity u, meridional velocity v, vertical velocity w, potential temperature θ, or salinity s. Unresolved fluctuations in these quantities are denoted as x', representing u', v', w', θ', and s', respectively. Horizontal processes (e.g., continuity, advection) on scales larger than a model domain (100 m in LES; all lengths in a one-dimensional vertical model) cannot be represented explicitly. However, the prognostic equations can be forced by prescribing such large-scale property features, denoted as upper case U, V, W, Θ, and S, respectively. An equation of state is used to derive density, ρ, and buoyancy, $b = g(1 - \rho/\rho_o)$, where g is gravitational acceleration and ρ_o is a reference density.

The K-profile parameterization of vertical mixing is intended for coarse resolution where the vertical fluxes, $\overline{w'x'}$, are not resolved. Within an oceanic boundary layer of depth h the physics of turbulent mixing is distinct from the interior below (Wyngaard 1982). Therefore, KPP distinguishes between the two regimes with a general form:

$$\overline{w'x'}(z) = \begin{cases} -K_x(z)(\partial_z x - \gamma_x), & -z \le h \\ -\nu_x(z)\partial_z x, & -z > h. \end{cases} \quad (1)$$

There is downgradient turbulent diffusion in both the interior ($-z > h$) and the boundary layer with ν_x and K_x the respective eddy coefficients. In the boundary layer, there is also a nonlocal turbulent transport that is governed by γ_x. This term is nonzero only for scalars (θ and s) in unstable (convective) forcing conditions, when it depends directly on the surface flux $\overline{w'x'}$ and inversely on h and the wind forcing (Large et al. 1994).

The vertical extent of the oceanic boundary layer depends on the surface forcing, the oceanic stratification, and shear. It can be very different than the depth of the isothermal layer, or mixed layer. Essentially h is a measure of how deep a boundary layer eddy, with a near-surface velocity and buoyancy, can penetrate into the interior stratification before becoming stable in a Richardson number sense, relative to the local velocity and buoyancy. Numerically it is the shallowest depth that a bulk Richardson number first exceeds a critical value, $\mathrm{Ri}_c = 0.3$. Complete details are given in Large et al. (1994).

In stable forcing (heating) conditions and at depths below the Monin–Obukhov depth L, buoyant suppression of turbulence exceeds the mechanical production and other sources of turbulent energy are small. Since there should not, therefore, be any surface-driven turbulent mixing at these depths, there is an option in the scheme to impose the restriction $h < L$ when the surface buoyancy flux B_f is into the ocean ($B_f > 0$). Numerically, L is computed as

$$L = u^{*3}/(\kappa B_f), \tag{2}$$

where u^* is the ocean friction velocity and $\kappa = 0.4$ is the von Kármán constant. This option is often not exercised because sensitivity studies have not shown a positive impact (Large et al. 1994).

The vertical mixing (1) in the ocean interior below the boundary layer ($-z > h$) is regarded as the superposition of three processes: local Richardson number instability due to resolved vertical shear, internal wave breaking, and double diffusion. Each process is parameterized in terms of a local vertical diffusivity, ν_x^s, ν_x^w, and ν_x^d, respectively. The profile of effective overall interior diffusivity then becomes

$$\nu_x(z) = \nu_x^s(z) + \nu_x^w(z) + \nu_x^d(z). \tag{3}$$

However, in all applications here double diffusivity is disabled by setting $\nu_x^d = 0$ at all depths. Interior mixing due to unresolved internal-wave shear is parameterized as

$$\begin{aligned} \nu_u^w &= \nu_v^w = 1.0 \times 10^{-4}\ \mathrm{m^2\ s^{-1}} \\ \nu_\theta^w &= \nu_s^w = 0.1 \times 10^{-4}\ \mathrm{m^2\ s^{-1}}, \end{aligned} \tag{4}$$

where the latter is consistent with the observational estimates of Ledwell et al. (1993).

Shear instability mixing occurs locally in stratified flow when the vertical velocity shear overcomes the stabilizing effect of the buoyancy gradient. The tendency for shear instabilities to develop is generally characterized by the local gradient Richardson number,

$$\mathrm{Ri}_g = \frac{\partial_z b}{(\partial_z u)^2 + (\partial_z v)^2}, \tag{5}$$

and turbulent mixing can ensue when Ri_g is below some critical value, Ri_o. The interior scheme of KPP parameterizes this mixing as a function of Ri_g that is the same for momentum and all scalars:

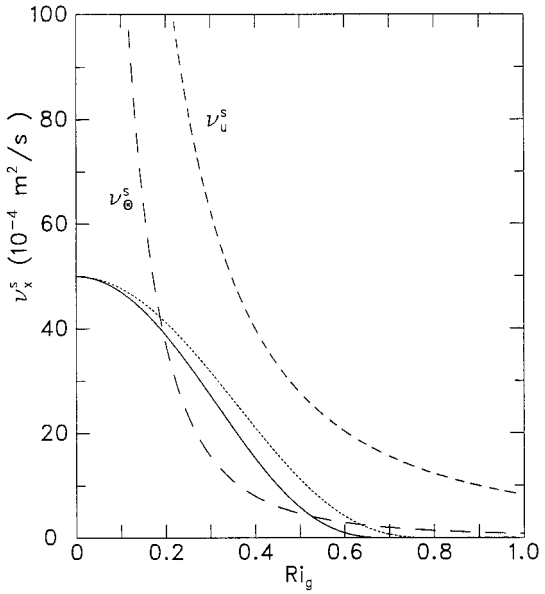

FIG. 1. Vertical viscosity and diffusivity for shear instability mixing as a function of gradient Richardson number; viscosity and diffusivity from (6) with $\mathrm{Ri}_o = 0.7$ (solid trace) and with $\mathrm{Ri}_o = 0.8$ (dotted trace) and viscosity from (7) (short dashed, ν_u^s) and diffusivity from (7) (long dashed, ν_θ^s).

$$\frac{\nu_x^s}{\nu^0} = \begin{cases} 1, & \mathrm{Ri}_g < 0 \\ \left[1 - \left(\dfrac{\mathrm{Ri}_g}{\mathrm{Ri}_o}\right)^2\right]^3, & 0 < \mathrm{Ri}_g < \mathrm{Ri}_o \\ 0, & \mathrm{Ri}_o < \mathrm{Ri}_g. \end{cases} \tag{6}$$

This parameterization is shown in Fig. 1 (solid line) for the values set by Large et al. (1994) ($\nu^0 = 50 \times 10^{-4}$ m^2 s^{-1}, $\mathrm{Ri}_o = 0.7$), but these choices have not been verified against observations in a systematic sensitivity study. Therefore, Fig. 1 (dotted line) also shows (6) for $\mathrm{Ri}_o = 0.8$.

We wish to compare results using the KPP scheme to results using the vertical mixing scheme that it has replaced in the equatorial, upper-ocean numerical model of Gent and Cane (1989). This latter scheme is documented in Gent (1991) and is hereafter referred to as the control (CON). The control mixing uses the KPP interior form (3) but applies it throughout the water column. The control internal wave mixing uses the KPP coefficients (4), and there is no double diffusion. Shear instability mixing is again a function of Ri_g but uses a formulation based on that of Pacanowski and Philander (1981). However, the values of the constants have been changed in order to fit the observations of Peters et al. (1988). The form is

$$\nu_u^s = \nu_v^s = 0.1(1 + 10\mathrm{Ri}_g)^{-2}\ \mathrm{m^2\ s^{-1}}$$
$$\nu_\theta^s = 0.1(1 + 10\mathrm{Ri}_g)^{-3}\ \mathrm{m^2\ s^{-1}}. \quad (7)$$

The functions ν_x^s from (7) are plotted in Fig. 1 along with the the KPP equivalent (6). The curves are quite different in several aspects. First, in the KPP scheme the viscosity and diffusivity are the same function of Ri_g, whereas (7) assumes rather different dependencies. Second, at small Ri_g, (7) gives much larger values of ν_u^s and ν_θ^s than the KPP scheme (6). The reason for this is that, in order to produce a mixed layer, (7) requires larger values in the near-surface region where it dominates the total vertical viscosity and diffusivity used in the Gent and Cane model. A mixed layer results from the large values of ν_u^s and ν_θ^s when Ri_g is less than 0.2. In the KPP scheme however, the large vertical mixing values in the boundary layer are set according to the other laws [see (1) and Large et al. (1994)], while equation (3) sets the mixing values only below the boundary layer. It is clear from Fig. 1 that (7) has much more momentum mixing than the KPP scheme below the boundary layer. The vertical diffusivities in the two cases are much more comparable, but the differences where $0.2 < \mathrm{Ri}_g < 0.5$ may be significant.

3. One-dimensional model comparisons with LES

Wang et al. (1998) utilized large eddy simulations to study the deep diurnal cycle of turbulence at the equator. Here we compare the results of their numerical experiments with those of the one-dimensional KPP mixing model described in Large et al. (1994). In the control integrations the same model is integrated but with the mixing implied by (3), (4), and (7) applied everywhere. The LES vertical resolution is 1 m over 270 m. In the comparative cases, the LES domain is 80 m square in the horizontal with 5-m resolution in their first configuration (LES I) and refined to 2.5 m in the third (LES III). Wang et al. (1998) primarily show the results of their second experiment, where the horizontal domain is 160-m square with 5-m resolution. The standard one-dimensional KPP and control vertical resolution of 4 m, is chosen to be about as high as a large-scale model could computationally afford. A KPP sensitivity experiment has 10-m vertical resolution, which is more typical of ocean general circulation models. The KPP and control model domains are always 200 m deep.

From identical prescribed initial conditions, LES I and all KPP and control experiments are integrated for 6 days (144 h) with identical surface forcing. The LES I solution at 1500 on day 5 is used as the initial condition for the 33-h integration of the much more computationally demanding high-resolution LES III. In all cases the applied wind stress is constant and zonal at -0.042 N m^{-2}, corresponding to a wind speed of about 5.4 m s^{-1} and $u^* = 0.0064$ m s^{-1}. There is a constant surface cooling of 200 W m^{-2} and a diurnal cycle of solar heating. This cycle is given by

$$I(0, t) = 776\ \mathrm{W\ m^{-2}}\ \sin[(2t - 0.5)\pi] \times \mathbf{H}\sin[(2t - 0.5)\pi], \quad (8)$$

where t is the time in days from the start of the integration at midnight on day 1 and **H** is the Heaviside step function. Absorption of solar radiation $I(z, t)$ is prescribed for moderately clear Jerlov type IB water (Jerlov 1976; Paulson and Simpson 1977). The daily average surface heating is 47 W m^{-2}. This average gives a daily turbulent temperature scale $\theta^* = 0.0018$ K, which satisfies $(\rho_o C_p)u^*\theta^* = 47$ W m^{-2}, where $\rho_o C_p = 4.1 \times 10^6$ J m^{-3} K^{-1} is ocean density times specific heat.

a. LES model

The complete set of LES model equations for the prognostic variables u, v, w, θ, and subgrid turbulent kinetic energy are given in Wang et al. (1998). Of these, the most relevant here are

$$\partial_t u + u\partial_x u = fv - \partial_x p + R_u + G_U$$
$$\partial_t v + v\partial_y v = -fu - \partial_y p + R_v + G_V$$
$$\partial_t\theta + u\partial_x\theta + v\partial_y\theta + w\partial_z\theta = -\partial_z\overline{w'\theta'} + (\rho_o C_p)^{-1}\partial_z I(z,t) + H_\Theta, \quad (9)$$

where p is pressure and f is the Coriolis parameter. Details of the parameterization of the subgrid Reynolds stress tensor components, R_u and R_v, and of $\overline{w'\theta'}$ are given in Wang et al. (1998). Except near the surface, the turbulent fluxes are largely resolved in LES, so there is relatively little sensitivity to these parameterizations and (1) is not applicable.

In (9), forcing by the unrepresented large scale is given by G_U, G_V, and H_Θ. The nonzero terms of these functions are

$$G_U = -u\partial_x U - W\partial_z u - \partial_x P + F_U$$
$$G_V = -v\partial_y V - W\partial_z v$$
$$H_\Theta = -u\partial_x\Theta - W\partial_z\theta + F_\Theta. \quad (10)$$

They are determined from the following prescribed profiles: the large-scale zonal pressure gradient $\partial_x P$, the zonal gradient of zonal velocity $\partial_x U$, the meridional gradient of meridional velocity $\partial_y V$, and the mesoscale eddy contributions to the zonal momentum and heat equations, F_U and F_Θ, respectively. Their values are estimated from ocean observations (Bryden and Brady 1989) and eddy-resolving tropical basin models (e.g., Gent and Cane 1989) by Wang et al. (1998), who show profiles of each as well as of the following derivatives. First, continuity is used to compute the large-scale vertical gradient of vertical velocity $\partial_z W$, which is then integrated to give the $W(z)$ of (10). Finally, the large-scale horizontal temperature gradients are determined by the hydrostatic relation

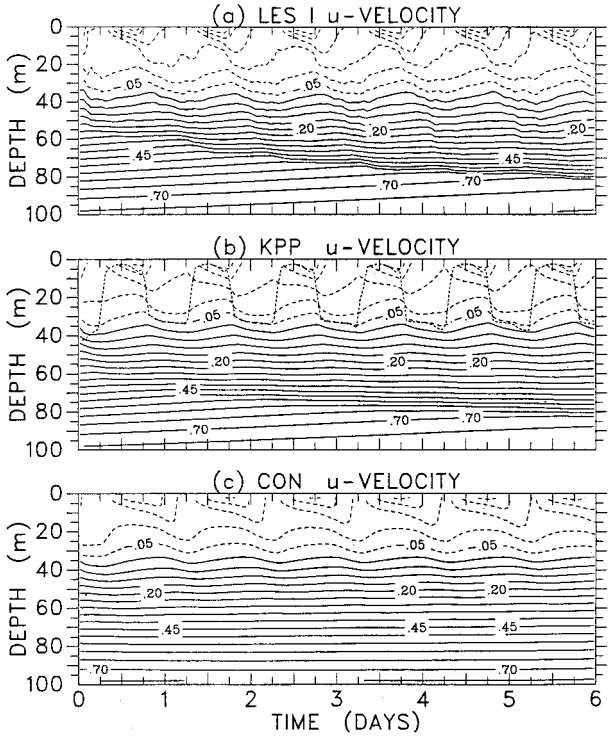

FIG. 2. Zonal velocity plotted as a function of time and depth over the upper 100 m only, with a contour interval of 0.05 m s^{-1}. (a) LES I solution, (b) standard KPP solution with boundary layer depth shown as the dotted trace, and (c) CON.

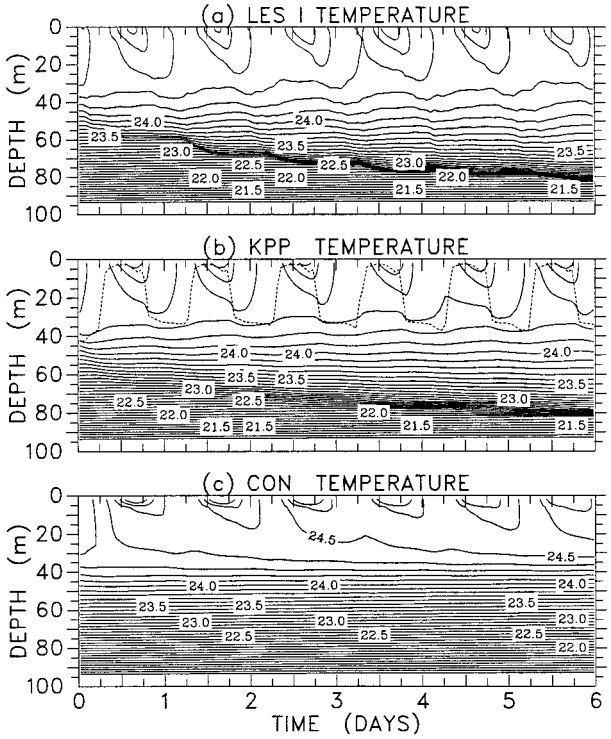

FIG. 3. As in Fig. 2 but for temperature with a contour interval of 0.1°C.

$$\partial_x \Theta = \frac{1}{\alpha g} \partial_{xz} P, \tag{11}$$

where $\alpha = 0.000\ 27\ \mathrm{K}^{-1}$ is the thermal expansion coefficient.

b. The 1D model

As detailed in Large et al. (1994), the 1D model discretizes and implicitly integrates the following prognostic equations:

$$\begin{aligned} \partial_t u &= \partial_z[-\overline{w'u'}] + fv + G_U \\ \partial_t v &= \partial_z[-\overline{w'v'}] - fu + G_V \\ \partial_t \theta &= \partial_z[-\overline{w'\theta'}] + (\rho_o C_p)^{-1} \partial_z I(z, t) + H_\Theta. \end{aligned} \tag{12}$$

Salinity is also prognostic in the model, but with no forcing it remains constant everywhere at its initial uniform value of 35 psu. Here there are no resolved turbulent eddies, and either the KPP scheme [(1), (3), (4), and (6)] or the Gent (1991) control mixing [(3), (4), and (7)] is used to parameterize the kinematic fluxes. The large-scale forcing is applied in the same manner as for LES (10) with identical profiles of $\partial_x P$, $\partial_x U$, $\partial_y V$, F_U, and F_Θ and their derivatives $W(z)$ and $\partial_x \Theta$.

Large et al. (1994) use midlatitude ocean observations and model simulations to determine standard values for the boundary layer parameters of KPP (e.g., $\mathrm{Ri}_c = 0.3$). All 1D KPP model results presented here use the same values. However, midlatitude conditions are not suitable for exploring interior mixing. Therefore the LES results are now used to determine suitable values for the interior mixing parameters of section 2. Wang et al. (1998) show LES values of viscosity and diffusivity as functions of gradient Richardson number Ri_g. These results at $\mathrm{Ri}_g > 1$ support the numerical values of (4).

These LES results are also consistent with having equal values of diffusivity and viscosity in the KPP parameterization (6) of shear instability mixing (Fig. 1). For small values of $\mathrm{Ri}_g < 0.1$, they also indicate that the limiting value of $\nu^0 = 50 \times 10^{-4}\ \mathrm{m}^2\ \mathrm{s}^{-1}$. However, at intermediate values of $0.1 < \mathrm{Ri}_g < 1.0$, the LES results are better represented with $\mathrm{Ri}_o = 0.8$ than the Large et al. (1997) value of 0.7. The effect of this change on the diffusivity and viscosity is shown in Fig. 1. It increases them by more than a factor of 2 for $0.5 < \mathrm{Ri}_g < 0.8$, and by about $5 \times 10^{-4}\ \mathrm{m}^2\ \mathrm{s}^{-1}$ at $\mathrm{Ri}_g = 0.4$. In the thermocline (e.g., depth 50 to 70 m), the great majority of LES values fall within the range $0.2 < \mathrm{Ri}_g < 0.6$, so significant sensitivity to Ri_o is possible.

c. Comparison of LES with standard KPP and control

The evolution of zonal velocity and temperature throughout the six-day integration of LES I, KPP, and CON are compared in Figs. 2 and 3. For clarity here and later, only the upper 100 m is shown. It is evident

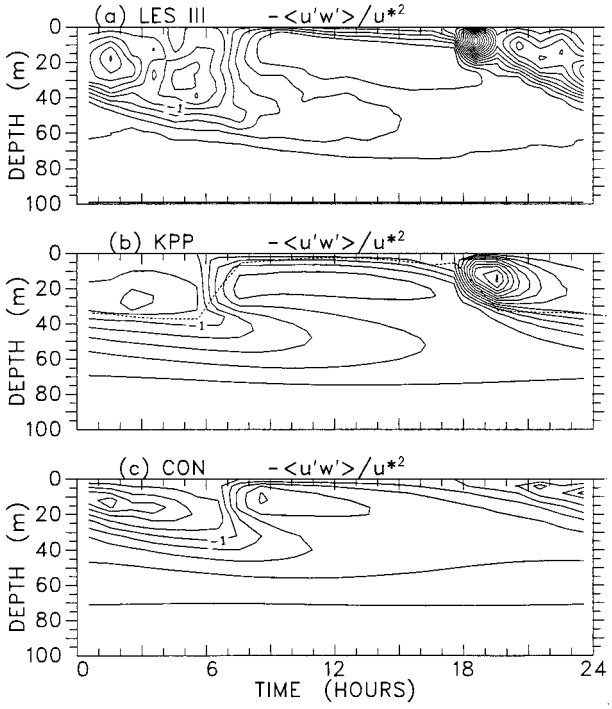

FIG. 4. The day 6 diurnal cycle of momentum flux plotted as a function of depth and normalized by $u^{*2} = 4.1 \times 10^{-5}$ m^2 s^{-2}, with a contour interval of 0.2. (a) LES III solution, (b) KPP solution, with boundary layer depth shown as the the dotted trace, and (c) CON.

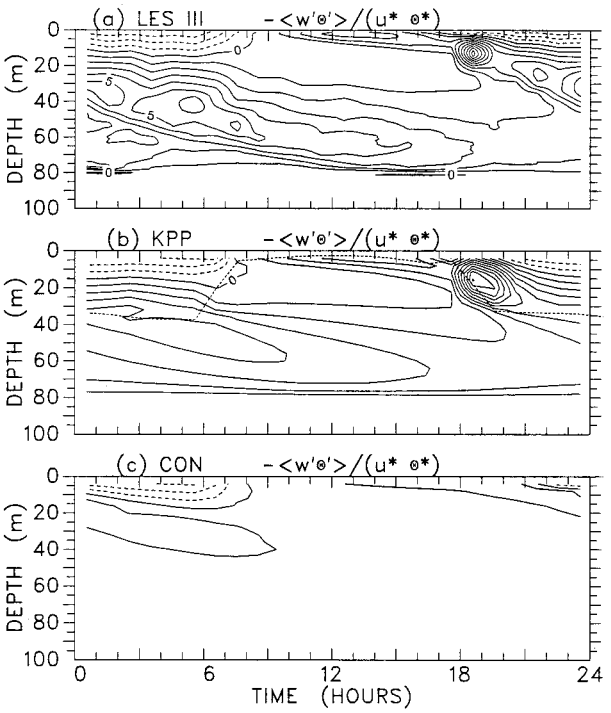

FIG. 5. As in Fig. 4 but for heat flux normalized by $u^*\theta^* = 1.15 \times 10^{-5}$ m s^{-1} K and a contour interval of 1.0.

that the prescribed large-scale forcing is only partially successful at balancing (9) and (12). The resulting trends are somewhat larger in temperature than in u. The Equatorial Undercurrent initially has a maximum speed of 0.8 m s^{-1} at about 110-m depth, but for both KPP and LES the core accelerates to about 0.82 m s^{-1} after 6 days because of a too large pressure gradient. This pressure gradient excess, and the upward diffusion of eastward momentum from the EUC results in the eastward acceleration of the deeper water evident in Fig. 2a and Fig. 2b. This acceleration is reversed by the penetration of westward momentum imparted by the wind stress. A companion heating is seen in Figs. 3a and 3b at depths where the surface heating is felt, with cooling above about 50 m. The rate of such vertical penetration is very similar in both LES I and KPP, reaching to about 82 m by the end of day 6. The control behaves differently, with negligible evolution below about 40 m and westward acceleration above 10 m where the wind stress is not completely balanced. There is also a heating trend between 10 and 40 m.

Distinct diurnal cycles in near-surface u and θ are evident in both Figs. 2 and 3. At the surface the amplitudes are damped by the 4-m resolution of the 1D model compared to the 1-m resolution of LES. Otherwise the KPP and LES solutions are similar. In both, there is a phase delay relative to the surface that increases with depth in both u and θ. This can be traced to at least 40 m where the delay is about 15 h. The boundary layer depth (Figs. 2b and 3b) varies from about 35 m at night to less than 5 m during the day, with rapid transitions of less than 2 h. In contrast, the control diurnal cycle is confined to shallower depths and the duration of warm daily SSTs is longer.

Even though the imbalances in (9) and (12) are not entirely rectified by the sixth day, the KPP and LES solutions are not diverging significantly, so the day 6 LES results can be meaningfully compared to the KPP model solutions. There is more divergence of the control solution. Figures 4 and 5 compare the day 6 diurnal cycles of momentum flux and heat flux, respectively, from the high-resolution LES III, the KPP, and the CON runs. The LES and KPP produce several common basic features. The onset of nighttime convection at about 1800 local time rapidly deepens the boundary layer and for a few hours produces intense fluxes at depth between about 5 and 20 m. Through the night, the strength of this flux maximum diminishes and its depth increases to about 50 m at sunrise. This feature can be traced throughout the next day, with its depth reaching about 65 m, and its strength continually weakening until it is reinforced by the next night's convection. Meanwhile, the solar-heating-induced stratification traps the surface-driven fluxes above about 10 m, leaving a pronounced minimum in the fluxes throughout the day at depth between about 10 and 30 m. Nighttime convection produces a temperature inversion only in the upper few meters in LES (Fig. 3a), a feature that is not resolved

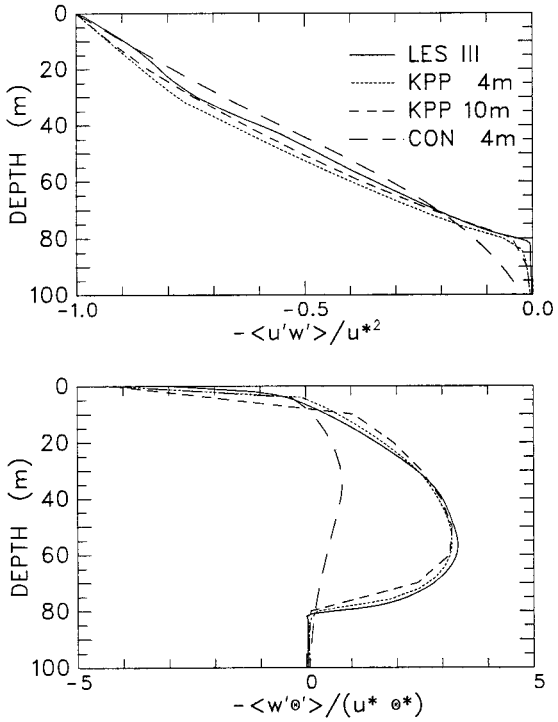

FIG. 6. Day 6 average depth profiles of (a) normalized momentum flux and (b) normalized heat flux. LES III solution (solid), standard KPP solution with 4-m resolution (dotted), KPP solution with 10-m resolution (short dashed), and CON with 4-m resolution (long dashed).

by KPP (Fig. 3b). Deeper to 15 m, $\partial_z\theta$ is positive, so the nighttime negative contours ($-\overline{w'\theta'} < 0$) in Figs. 5a and 5b indicate countergradient heat flux, which in the KPP scheme is due to the nonlocal term in (1).

In the control (Fig. 4c and Fig. 5c) there is no evidence of intense convection at sunset. Nighttime cooling does appear as cores of high momentum and heat flux, but these tend to be shallower than the LES feature throughout the diurnal cycle. The heat flux at depth is also much weaker. The delayed onset of increased heat fluxes until about 2100 is the reason why the high daily SSTs persist so long in Fig. 3c. The region of negative heat fluxes in Fig. 5c is less extensive than in both LES and KPP. Such fluxes can only occur where there is a temperature inversion (Fig. 3c) because the control only has downgradient heat flux. In general, the diurnal cycle of momentum flux in the control is more similar to LES (Fig. 4) than is the heat flux (Fig. 5). This is likely a consequence of the viscosity in (7) being so much larger than the diffusivity (Fig. 1).

There are differences in detail in the daily cycle of KPP and LES fluxes, but for long integrations it is important that a mixing scheme produce daily average fluxes that are comparable with those of LES. Figure 6, which shows profiles of day 6 average fluxes, demonstrates that this is so for the KPP scheme but not for the control run. Below about 80-m depth the fluxes become negligible, except for the control momentum flux. Above, the momentum flux divergence produces westward (negative) acceleration because of the wind in all cases. In LES and KPP the heat flux divergence tends to heat the water between 60 and 80 m. There is a general cooling higher, especially above about 5 m, where this turbulent heat flux tends to balance the radiative solar heating. Wang et al. (1998) show the corresponding profiles from their other LES experiments, and these differ from LES III (Fig. 6) by more than either the standard KPP or the coarse 10-m resolution KPP solutions. The major discrepancy in Fig. 6 is that the control run heat flux is much too weak from about 10 m to nearly 80 m depth.

d. KPP sensitivity to interior mixing

The evolution of upper-ocean temperature in these models is governed by the surface heat flux, the prescribed large-scale forcing, and the entrainment of colder water from below. In the midlatitude cases explored by Large et al. (1994), this entrainment was dominated by the boundary layer depth, so solutions were very sensitive to boundary layer parameters such as Ri_c. In the equatorial environment, however, the entrainment depends more on the interior mixing and is most sensitive to the shear instability parameterization (6). Decreasing Ri_o from 0.8 to the Large et al. (1994) value of 0.7 reduces this entrainment. With less cold water, the day 6 upper-ocean temperatures are about 0.03°C warmer throughout all phases of the diurnal cycle. In contrast, increasing Ri_o from 0.8 to 1.0 enhances the entrainment and results in a cooler, by about 0.08°C, upper ocean on day 6.

In addition to the LES III and standard KPP profiles of Fig. 6, Fig. 7 shows day 6 average flux profiles for two other KPP integrations; one with $\mathrm{Ri}_o = 0.7$ and the other with $\mathrm{Ri}_o = 1.0$. A useful measure of the degree of entrainment is the depth at which the fluxes approach their background levels. Using $\overline{u'w'} = 0.05u^{*2}$ as a practical definition, this depth is 79, 82, and 88 m, for the cases $\mathrm{Ri}_o = 0.7$, 0.8, and 1.0, respectively, and 80 m for LES III. Using $-\overline{w'\theta'} = 0.5u^*\theta^*$ gives 79, 80, and 87 m for the respective KPP depths and 80 m for LES III. In this regard $\mathrm{Ri}_o = 0.7$ and 0.8 compare equally well with LES III, but $\mathrm{Ri}_o = 1.0$ results in too much entrainment. The strongest support for using $\mathrm{Ri}_o = 0.8$ is the close agreement with the LES III heat flux between 20 and 80 m.

Larger values of ν^0, the maximum diffusivity and viscosity at $\mathrm{Ri}_g = 0$ in the shear instability parameterization (6), give larger mixing coefficients at all Ri_g less than Ri_o. However, the effect on entrainment near 80-m depth is small. Instead, the sensitivity of KPP equatorial solutions to ν^0 is surprising and dramatic, as shown in Fig. 8. The corresponding diurnal cycles of heat flux display a similar sensitivity, so are not presented. As ν^0 is increased, the onset of the vigorous

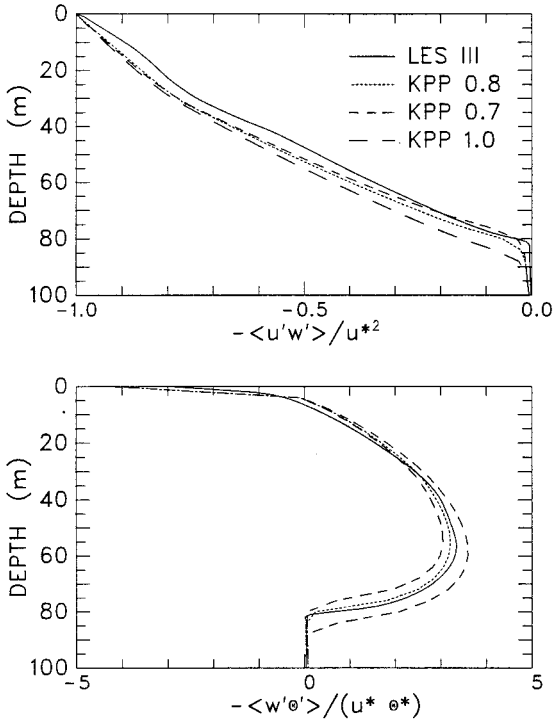

FIG. 7. As in Fig. 6 but only for KPP with 4-m resolution. LES III solution (solid), $Ri_o = 0.8$ (dotted), $Ri_o = 0.7$ (short dashed), and $Ri_o = 1.0$ (long dashed).

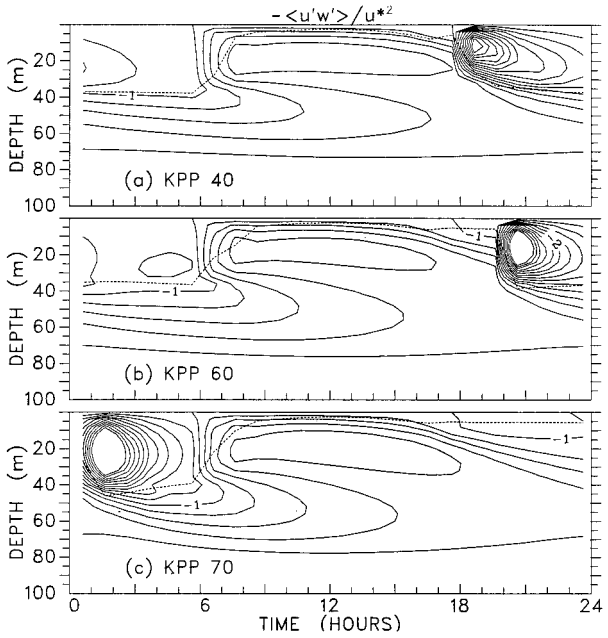

FIG. 8. The day 6 diurnal cycle of normalized momentum flux plotted as a function of depth for 4-m resolution KPP solutions (a) $\nu^0 = 40$, (b) $\nu^0 = 60$, and (c) $\nu^0 = 70 \times 10^{-4}$ m² s⁻¹. In all cases the contour interval is 0.2 and contours greater than 3.0 are not shown.

nighttime convection and rapid deepening of the boundary layer depth occurs later and later. For $\nu^0 = 40$ (Fig. 8a) to 50 (Figs. 4 and 5) $\times 10^{-4}$ m² s⁻¹ the onset is around 1800, as in LES III. However, at $\nu^0 = 60 \times 10^{-4}$ m² s⁻¹ the onset is appreciably later with the rapid deepening beginning after 1930 (Fig. 8b). A further increase to $\nu^0 = 70 \times 10^{-4}$ m² s⁻¹ delays the onset and deepening much longer, to just after midnight. This case has some similarity to the control, Fig. 4c and Fig. 5c. The large shear instability mixing appears to be capable of balancing the convective nighttime surface cooling, without convective deepening of the boundary layer. But without the vigorous mixing the surface cooling is much slower (0.1°C in 3.5 h vs 0.1°C in 1 h). Also, the surface current remains nearly constant until midnight instead of slowing from 22 to 20 cm s⁻¹ between 1800 and 1900. Other aspects of the diurnal cycle are similar to Figs. 8a and 8b because they are governed primarily by the solar heating, which is identical in all cases. These features include the boundary layer shoaling between 0530 and 0800, as well as the daytime boundary layer depth, surface velocity, and surface temperature.

Numerous other sensitivity experiments were performed. In particular, these showed the short-term KPP equatorial solutions to be insensitive to the interior mixing due to unresolved internal-wave shear (4) and to whether or not the Monin–Obukhov depth (2) restriction was applied.

4. Three-dimensional numerical model

A reduced-gravity, general circulation model of the upper equatorial ocean is documented in Gent and Cane (1989). It was designed to address problems on the interannual timescale where only the upper ocean is important. The active model depth varies in both time and space, but the average is 400 m. The base of the active model is the 10°C isotherm, which is also an isopycnal surface in this model with no salinity variable. The vertical discretization was chosen such that the upper model level has a constant depth. The remaining layers are based on a sigma coordinate, which divides the depth between the base of the upper layer and the active model base into prechosen fractions. This allows for more resolution in the strong thermocline than elsewhere in regions where the vertical temperature gradient is much weaker. Full details can be found in Gent and Cane (1989), and the model was used to study the heat budget of the western Pacific Ocean in Gent (1991).

We will show results from two runs of the Gent and Cane model that have been run long enough so that the annual cycle is very similar over the last five years of integration. The runs differ only in the vertical mixing schemes used. As with the 1D model, the first is a control, which uses the Gent (1991) vertical mixing given by (4) and (7), and the second uses the KPP scheme (6). Both use 15 layers, with the upper layer having a fixed depth of 10 m. The average depths of the remaining layers vary monotonically between 10 and 50 m for the bottom layer. The horizontal resolution is the

same in both runs being 1° in the zonal direction and varying in the meridional direction between ¼° at the equator to 1° at the model boundaries at 30°N, S. The temperatures at the north and south boundaries are set to observed values.

Both runs use are forced by mean annual cycles from 4 years (1985–88). The mean monthly wind stress is determined from wind components from the global National Centers for Environmental Prediction Reanalysis (Kalnay et al. 1996). The bulk forcing detailed in Large et al. (1997) is used for the heat flux Q:

$$Q = Q_{\text{sol}} - Q_{\text{lat}} - Q_{\text{sen}} - Q_{\text{lw}}, \tag{13}$$

where the penetrating solar radiation is given by

$$Q_{\text{sol}} = (1 - A)Q_o f_1 \tag{14}$$

and its absorption with depth is as in section 3. In (14) $A = 0.07$ is the albedo, Q_o is the monthly surface insolation from version 2 of the International Satellite Cloud Climatology Project (Bishop and Rossow 1991), and f_1 is a constant factor that will be discussed below. The latent and sensible heat fluxes are given by

$$Q_{\text{lat}} = \rho_a C_T L|\mathbf{u}|[q(\text{SST}) - s_a f_2], \tag{15}$$

$$Q_{\text{sen}} = \rho_a C_T C_P|\mathbf{u}|(SST - T_a), \tag{16}$$

where the constants are $L = 2.5 \times 10^6$ J kg^{-1}, $\rho_a =$ 1.2 kg m^{-3}, $C_P = 1004$ J kg^{-1} K^{-1}; and $C_T = 0.0012$. The function q gives the saturation specific humidity. The mean annual cycles of wind speed $|\mathbf{u}|$, air temperature T_a, and the specific air humidity s_a are also from NCEP Reanalyses, and f_2 is a second constant to be discussed below. The longwave heat flux is given by

$$Q_{\text{lw}} = \epsilon\sigma T_a^3\{T_a[0.39 - 0.05(s_a f_2/0.62)^{1/2}](1 - 0.53C^2) + 4(\text{SST} - T_a)\}. \tag{17}$$

The mean annual cycle of fractional cloud cover, C, is taken from ISCCP data (Rossow and Schiffer 1991). The formula (17) comes from Berliand and Berliand (1952) (see Fung et al. 1984), where $\epsilon = 1.0$ is the emissivity and σ is the Stefan–Boltzman constant.

Large et al. (1997) show that, if the factors f_1 and f_2 are unity, and observed SST is used in Eqs. (15)–(17), then the globally averaged net heat flux into the ocean is about 50W m^{-2}. This unrealistic value was brought close to the desired value of zero by reducing the solar insolation by 12.5% ($f_1 = 0.875$) and the specific air humidity by 7% ($f_2 = 0.93$). These choices are somewhat arbitrary although there is observational evidence to support reduced values of solar insolation and specific air humidity. It was decided to use the same fields to force this regional model as Large et al. (1997) used to force a global ocean model.

The surface temperature and velocity fields in the two runs are very similar with differences in SST less than 1°C. The differences in the zonal surface velocity are mostly less than 10 cm s^{-1}. However, there are larger differences in the vertical profiles of temperature and velocity between the two runs. Therefore, we have chosen to compare the model results with the well measured Tropical Ocean and Global Atmosphere–Thermal Array for the Ocean (TOGA–TAO) observations. The longest data records on the equator are at 165°E, 170°W, 140°W, and 110°W.

Figure 9 compares the annual mean zonal velocity as a function of depth from the two model versions to TOGA-TAO data at the four locations along the equator. The TOGA-TAO current meter data are described in McPhaden and McCarty (1992). The figure shows that at 165°E and 170°W the equatorial undercurrent is considerably too strong above 150 m in both runs. The runs agree better with the data below 200 m, but tend to be too weak. At 140°W, the control run has a too strong undercurrent above 100 m, and the KPP run agrees well with the data. However, at 110°W the opposite is true with the control run having a somewhat better profile in the upper 70 m.

Figure 10 is similar to Fig. 9 but shows temperature rather than zonal velocity. Both profiles are very good at 165°E, even though both have somewhat too warm SSTs. At 170°W the KPP run has a somewhat better profile than the control run and agrees very well with the data. However, at 140°W the reverse is true with the control run being closer to the data, having a very good profile above 100 m but being too warm between 100 and 200 m. At 110°W both runs give a poor comparison with the data below 50 m, even though the control run is quite good in the upper 30 m.

We conclude from Figs. 9 and 10 that the control and KPP runs have about equal skill in reproducing the TOGA-TAO annual means. However, this skill is not high for zonal velocity in the western Pacific and for temperature in the eastern Pacific. Thus, we conclude that trying to differentiate between vertical mixing schemes in the context of a GCM by comparing to observations is not straightforward. The reasons are that the wind stress and heat flux forcings of the equatorial Pacific are not known exactly, and the GCM has deficiencies not related to the vertical mixing scheme, such as no salinity variable. We believe that the large deficiencies in both runs compared to TOGA-TAO data are not due to the vertical mixing schemes used in the model.

Figure 11 shows the SST anomaly, relative to the local annual mean, along the equator from the observations of Reynolds and Smith (1994) and from the KPP run. The model does quite well in reproducing the observations, although there is room for improvement. The magnitude of the annual cycle in the eastern Pacific is about 4°C in the model, whereas it is close to 5°C in the observations. Also the model has a too strong annual cycle in SST in the western Pacific. The annual cycle of SST in the control run is very similar to that in the KPP run, so is not shown. This similarity also suggests that deficiencies are not due to vertical mixing. Furthermore, Chen et al. (1994b) show a very similar an-

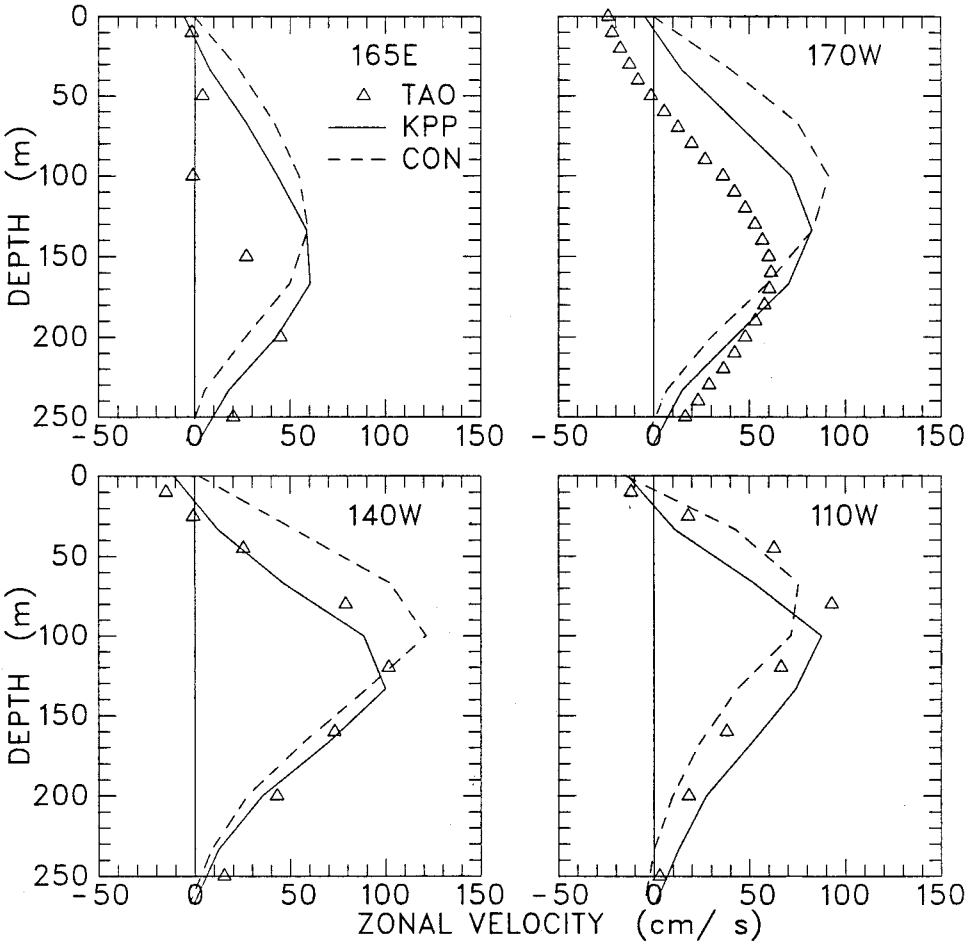

FIG. 9. Annual mean zonal velocity plotted against depth at 165°E, 170°W, 140°W, and 110°W. TOGA–TAO data (triangles), KPP run (Solid), and control run without KPP (dashed).

nual cycle of SST anomaly in the Pacific using their vertical mixing scheme. Thus, the question we address now is whether the good annual cycle of SST in these runs has been built in because of the heat flux formulation.

5. The heat flux formulation

Seager et al. (1988) hypothesize that air temperature is determined by SST, so it should not be included in heat flux parameterizations such as (15)–(17). The concern is that to do so overly constrains the model to produce the correct SST. If this is true, then the success of a model run at simulating the observed annual cycle of SST could be attributed to the way in which the heat flux was formulated. However, the mean annual SSTs from both model runs in Fig. 10 are as much as 1°C warmer (165°E and 110°W) than observed. Also, the heat flux typically depends much more on specific humidity (15) than air temperature, so even if SST does determine air temperature, it may not exert much control over the specific humidity and hence the heat flux.

In order to explore this issue further, we will show results from two additional simulations using the Gent and Cane model with the KPP parameterization scheme. In the first run, as in Seager et al. (1988) and Chen et al. (1994b), the atmospheric temperature is specified as an empirical function of SST. We use a fit to observations of T_a and SST along the equator in the Pacific Ocean:

$$T_a = (5\mathrm{SST} + 22)/6, \tag{18}$$

where all temperatures are in °C. Assuming a constant relative humidity of 75% and $f_2 = 1$ then eliminates NCEP T_a and s_a from the heat flux parameterizations (15)–(17). Use of this heat flux is referred to as SST forcing.

The second additional run is a 10-yr integration where the Gent and Cane tropical Pacific model with KPP is run in fully coupled mode with the (NCAR) Community Climate Model (CCM3). CCM3 and its dynamical results are documented in Hurrell et al. (1998). Both these models are component models in the NCAR Climate System Model (CSM) so that they can be integrated in

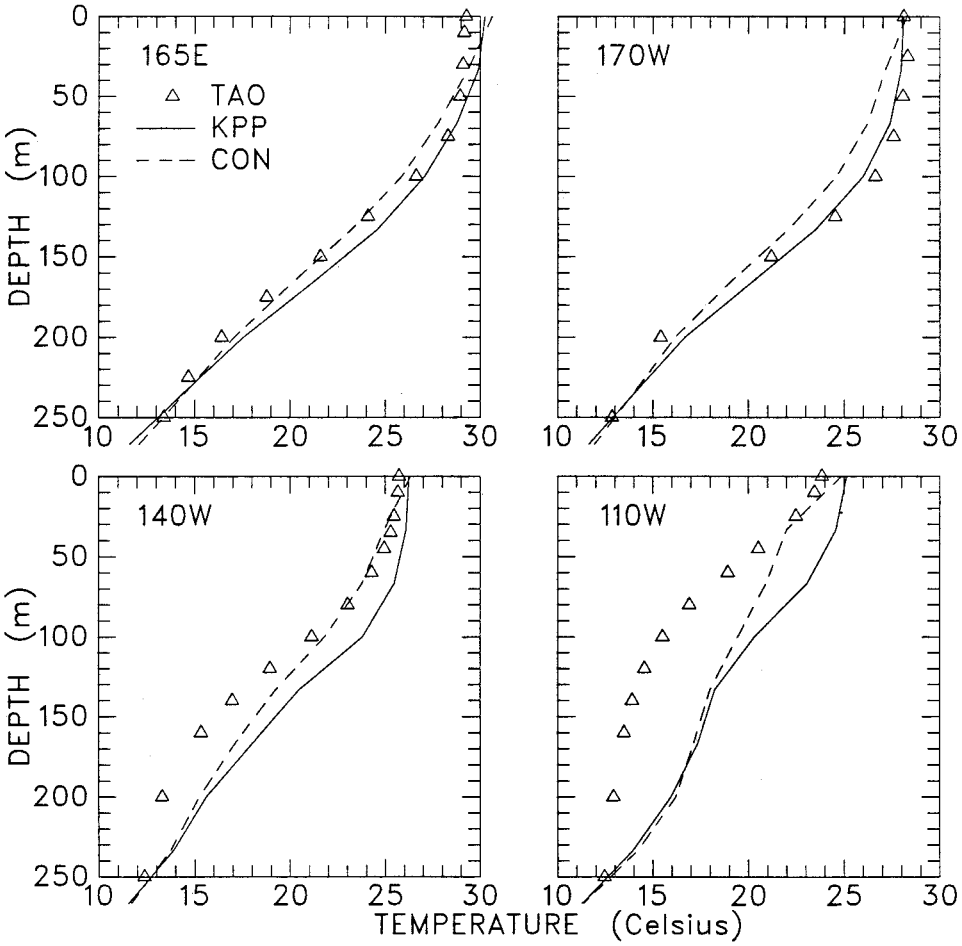

FIG. 10. As in Fig. 9 but for temperature.

coupled mode using the CSM Flux Coupler, which is documented in Bryan et al. (1996). Both wind stress and heat flux evolve during this coupled CSM run because they are calculated using the evolving atmospheric and SST fields. The solar and longwave heat fluxes are determined by the atmospheric model and are not given by (14) and (17).

Figures 12 and 13 show comparisons of the annual mean zonal velocity and temperature from the SST and CSM runs with TOGA-TAO observations at 165°E, 170°W, 140°W, and 110°W on the equator. Also shown for reference are the KPP results from Figs. 9 and 10. A major point we wish to emphasize is that changing to SST forcing has very little impact on these annual means. Bulk forcing with prescribed air temperature and specific humidity results in a significantly better mean SST only at 170°W. Much larger differences occur in the fully coupled CSM run, and in some instances these changes are larger than those between the control and KPP runs shown in Figs. 9 and 10. This illustrates that these solutions are rather sensitive to changes in the wind stress forcing, which has changed in the CSM run. This sensitivity is one of the difficulties in drawing conclusions about vertical mixing schemes by comparing GCM results with observations.

All the model runs produce too strong eastward zonal velocity above the EUC at 165°E and 170°W, even though the temperature profiles are in relatively good agreement. At 165°E the CSM result is 20 to 30 cm s^{-1} faster than the other model results and is very different than the observations. At 140°W and 110°W the zonal velocities from all the runs in Fig. 12 are in reasonable agreement with the observations but the temperature profiles are not. In particular, there is a bias toward warmer temperatures at all depths, especially at 110°W where the SST and KPP thermoclines are much too weak. Overall in the CSM run, where the heat flux is free of imposed constraints, the temperature profiles are closest to observations.

Figure 14 shows the SST anomaly, relative to the local annual mean, along the equator from the SST and CSM runs. Comparing Figs. 14a and 11b shows that in the eastern Pacific the largest effect of switching to SST from bulk forcing is a phase delay in the annual cycle of SST anomaly by about one month in the maximum to mid April and in the minimum to mid November.

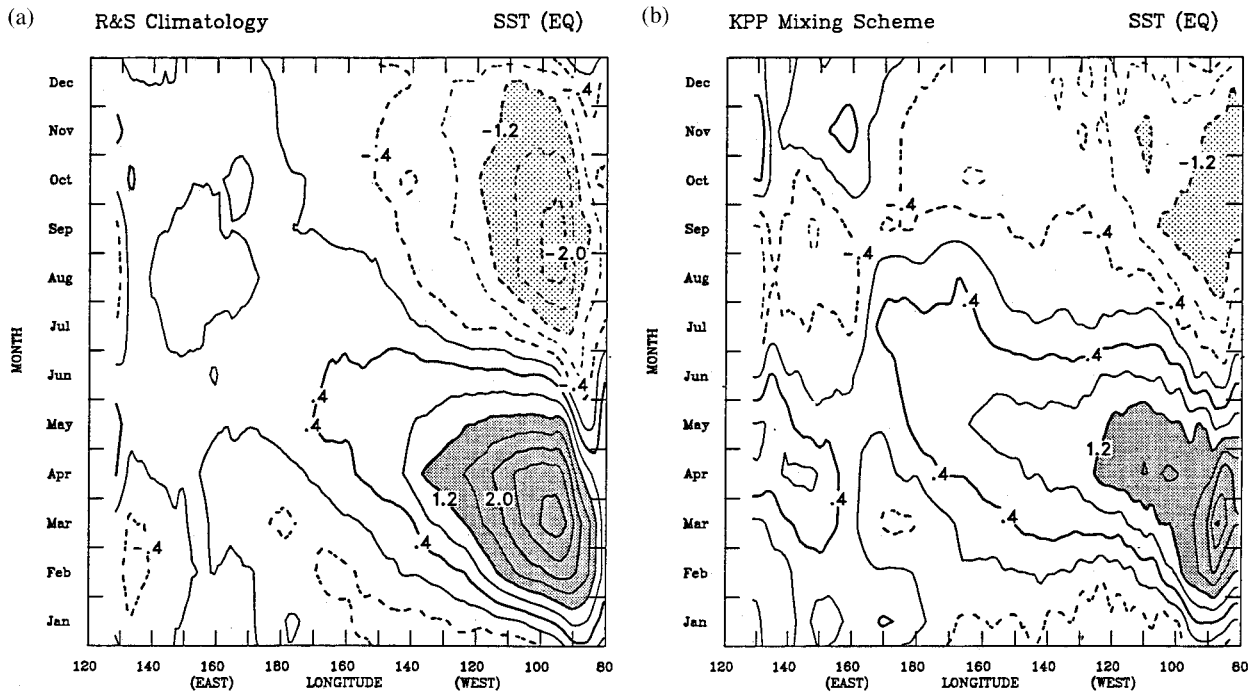

FIG. 11. The monthly SST anomaly relative to the local annual mean, along the equator plotted against longitude and time, with a contour interval of 0.4°C. (a) Observational analysis of Reynolds and Smith and (b) run with KPP.

The maximum is reduced by about 0.4°C but the minimum is colder by about the same amount, so the annual range remains about the same. Also, the area of SST anomaly greater than 1.2°C is confined east of about 90°W. In several respects the annual cycle of SST anomaly in the fully coupled CSM run (Fig. 14b) compares most favorably of all the runs to observations (Fig. 11a). In the east the maximum occurs in mid March between 90° and 100°W. The minimum occurs around the beginning of September, also between 90° and 100°W. The range of the annual cycle is more than 4°C but is still about 1°C too small.

West of the date line the annual cycle of SST anomaly in all the model runs begins to display the sun's semiannual passage, with maxima around May and November and mimima in the January–February and August–September time frames, and in all cases the range is much larger than observed. The SST forcing run is the poorest in this regard, with first maximum exceeding 1.2°C and second minimum below −1.2°C at many longitudes. The CSM run is not much better with a −1.2°C second minimum and a second maximum of more than 0.8°C at many longitudes.

6. Discussion and conclusions

Philander et al. (1987) published one of the first simulations of the tropical Pacific Ocean using a general circulation model. In the discussion section they state that ''This paper uses the most sophisticated model available, a general circulation model which simulates the tropical ocean realistically, provided accurate surface winds force the model. This proviso precludes a detailed comparison between the results presented here and measurements in the tropical Pacific Ocean.'' Although the Gent and Cane (1989) equatorial Pacific GCM has comparable sophistication, it cannot be demonstrated that with accurate forcing the model would simulate the equatorial ocean realistically. Consistent with the above Philander proviso, comparisons of model results and observations are insufficient support for such a statement. Indeed, several aspects of the model could be improved: the addition of salt, better inflow and outflow lateral boundary conditions especially near the coast of South America and the Indonesian Throughflow, and a cooler bottom boundary condition. Therefore, we first utilized large eddy simulations for a clean, direct demonstration of the fidelity of KPP vertical mixing in the equatorial regime where the parameterization had not been tested before. A companion control solution with vertical mixing based on the Pacanowski and Philander (1981) formulation revealed several shortcomings relative to the LES solution.

The demonstrations are presented in section 3 where results from the one-dimensional model described in section 2 are compared with the Wang et al. (1998) LES of the upper equatorial ocean. Prescribing the large-scale flow ensures that the LES and 1D models solve essentially the same set of equations. Then the identical surface forcing produces a clean comparison. The LES

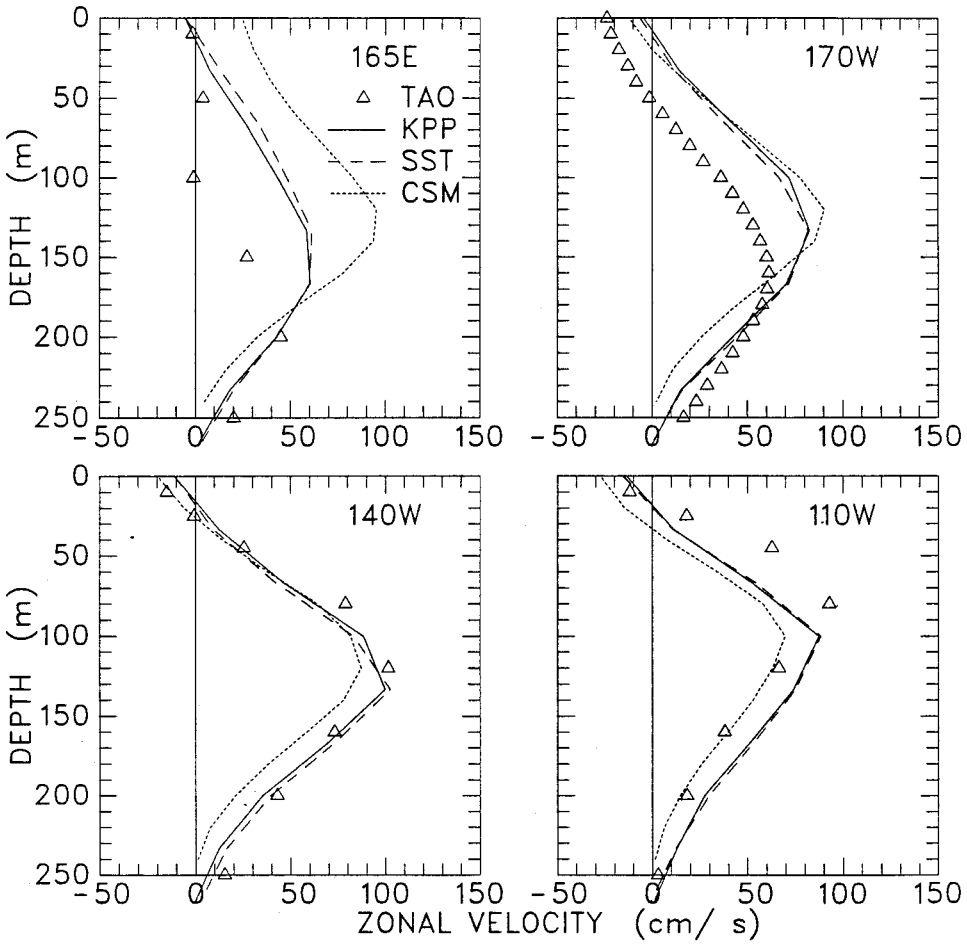

FIG. 12. Annual mean zonal velocity plotted against depth at 165°E, 170°W, 140°W, and 110°W. TOGA–TAO data (triangles), KPP run as in Fig. 9 (solid), SST forcing (dashed), and CSM fully coupled atmospheric GCM (dotted).

also offers the advantage of explicitly computed fluxes for direct comparison to parameterized vertical fluxes (1). The boundary layer depth in the KPP scheme is seen to shoal rapidly in response to the onset of solar heating and to deepen as rapidly in the convective conditions following sunset. This diurnal cycle produces near-surface temperature and velocity cycles that are very much like the LES, with the differences attributable to vertical resolution. A notable boundary layer feature of both models is the countergradient heat flux that accompanies nighttime convection and supports including a nonlocal term in (1). In contrast, the control solution failed to reproduce the intense convection at sunset, which impacted the diurnal cycle and confined the core of maximum heat flux to shallower depths than the LES solution. In the daily average these problems lead to control heat fluxes that are much too weak. Happily KPP at both 1- and 10-m vertical resolution agree much better with LES daily average fluxes. These results strongly suggest that in order to reproduce LES mixing, model physics is much more important than model resolution.

A unique feature of the equatorial ocean is the very large vertical shear in zonal velocity that is a consequence of the EUC. This shear is essential for the vertical propagation of turbulent fluxes from the region of convection. This propagation from 20 to 60 m in LES is observed as a diurnal cycle of turbulent dissipation (e.g., Gregg et al. 1985; Moum and Caldwell 1985). Vertical mixing in this region is dominated by shear instability, and the propagation is captured by the KPP parameterization. The warming associated with the mixing from above tends to increase the local stratification, but the associated mixing of westward momentum increases the local shear. The latter effect dominates the former in the calculation of the gradient Richardson number, which decreases. Consequently, the vertical mixing coefficients increase, which combine with the enhanced vertical gradients to increase the fluxes. The best comparison is achieved when the two parameters, ν^0 and Ri_o, are set to $\nu^0 = 50 \times 10^{-4}$ m^2 s^{-1} and $\mathrm{Ri}_o = 0.8$. The latter is a small change from the value proposed in Large et al. (1994) of 0.7. With these values,

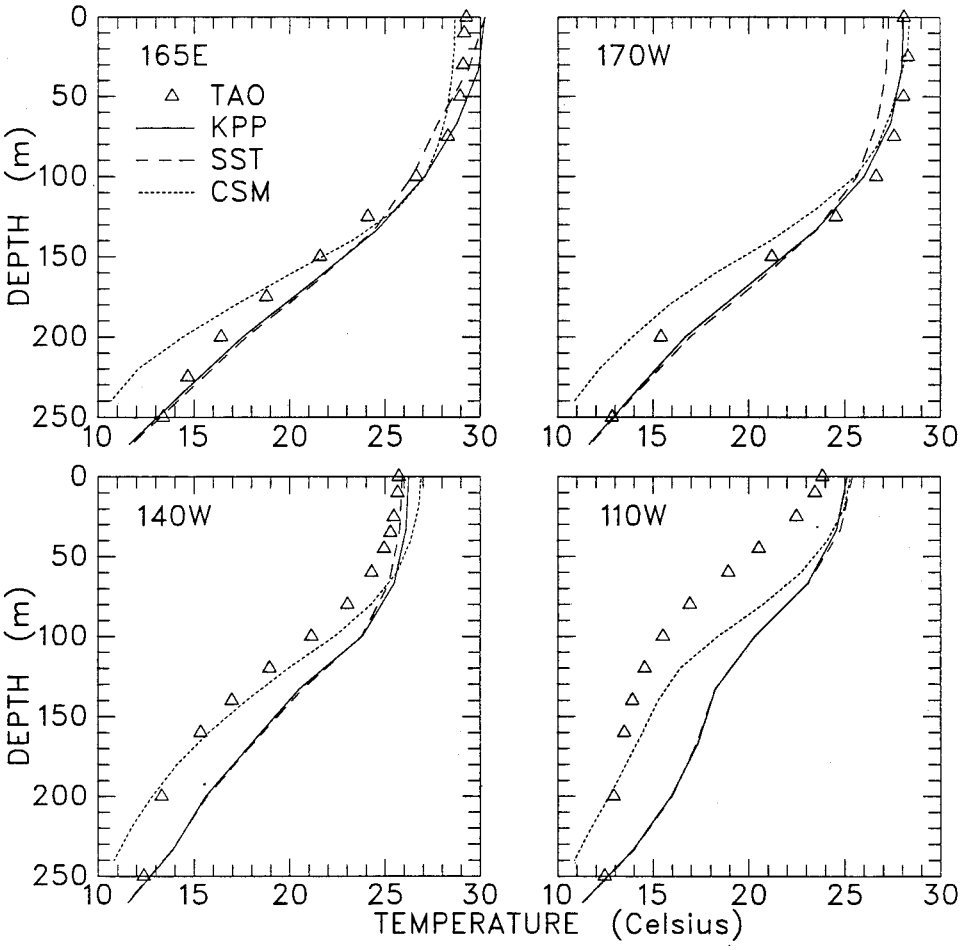

FIG. 13. As in Fig. 12 but for temperature.

the KPP mixing coefficients become consistent with the plots of viscosity and diffusivity as functions of gradient Richardson number in Wang et al. (1998), with values greater than 50×10^{-4} m^2 s^{-1} coming from the boundary layer.

Compared to the one-dimensional comparison of section 3, the equatorial Pacific comparisons of section 4 are neither as clean, because the correct ocean forcing is not known exactly, nor as direct, because there are no direct observations of equatorial ocean fluxes. Nevertheless, model simulations with and without the KPP scheme for vertical mixing are compared to each other and to observations. Although we sympathize with the Philander et al. (1987) proviso, these comparisons are meaningful because KPP performance is established independently using LES. From these comparisons it is concluded that the KPP scheme and the original vertical mixing scheme in the Gent and Cane (1989) model can do comparably well in reproducing the TOGA-TAO observations along the equator in the Pacific. It is unlikely that results with the Chen et al. (1994a) hybrid mixing scheme would be much different. There are two main biases in the annual means of all the model solutions. In the west, the eastward zonal flow is much too strong with a maximum that is too shallow. In the east, the thermocline is too weak with the model temperatures too warm at depth. There are also common biases in the annual cycle of SST along the equator. The amplitude is too small in the east and too large in the west. The persistence of these biases using very different vertical mixing schemes suggests that mixing is not primarily responsible.

The effect of using atmospheric temperature and humidity as functions of SST and of using full coupling to an atmospheric model is documented in section 5. From these and the control and KPP runs, where bulk forcing provides the most constraint on model SST, we conclude that specifying atmospheric temperature and humidity in the heat flux formulation is not a strong constraint on either model SST or subsurface temperatures, with the annual cycle of SST anomaly west of the date line a possible exception. The basis of this conclusion is that going from SST forcing to bulk forcing results in very small differences in mean temperature and velocity at all depths, including the surface (Figs. 12 and 13). There is some improvement in the annual

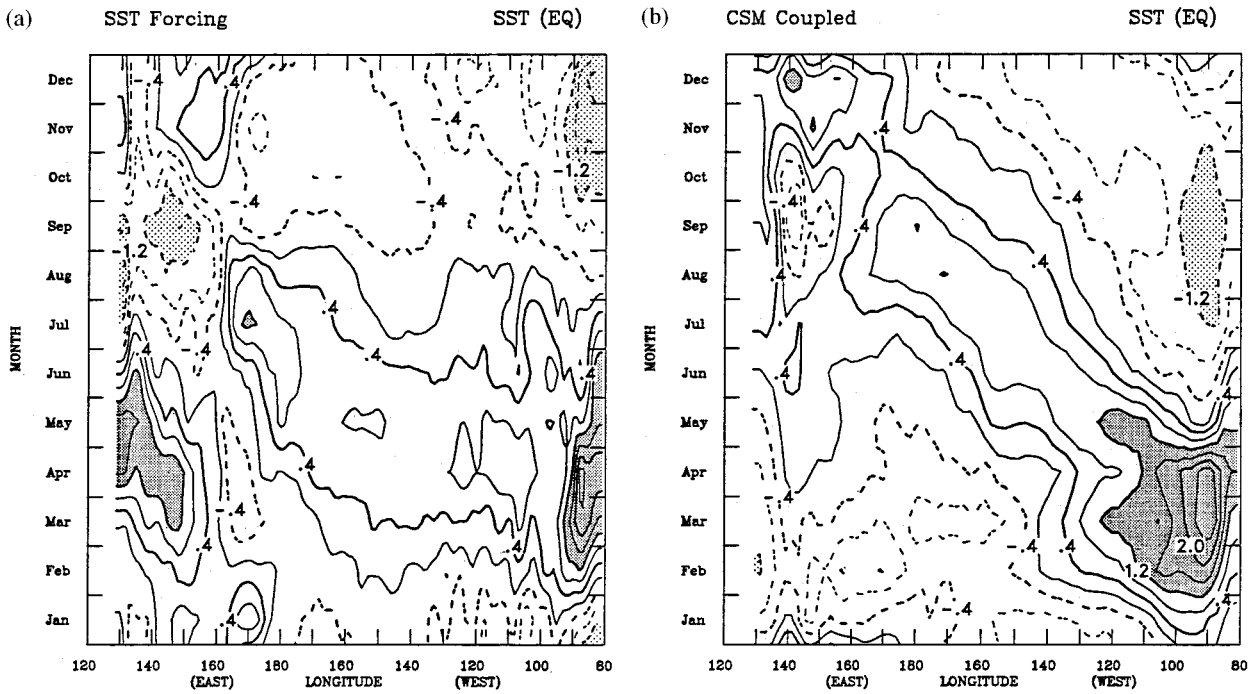

FIG. 14. The monthly SST anomaly, relative to the local annual mean, along the equator plotted against longitude and time. (a) SST forcing with T_a a function of model SST and (b) CSM fully coupled atmospheric GCM.

cycle of SST anomaly, namely phase in the east and amplitude in the west, but tuning the functional relation (18) could diminish these differences. There are no prescribed constraints in the coupled CSM case, yet it is very much like the bulk forced solution and observations in several respects: vertical temperature structure at 165°E, 170°W, and 140°W; zonal currents at 140° and 110°W; annual cycle of SST anomaly east of the date line; and a too strong semiannual cycle west of the date line.

Overall, the coupled CSM case provides one of the better comparisons with observations of temperature. This somewhat surprising and encouraging result, when combined with previous studies (e.g., Large et al. 1994), and with the ability of the one-dimensional KPP model to simulate the diurnal cycle of LES flux profiles, gives us confidence in the KPP scheme. Therefore, it is now standard in the Gent and Cane model and the global ocean model that are the two choices for the ocean component of the NCAR Climate System Model.

Acknowledgments. We are grateful to Dailin Wang for providing the LES model results and valuable comments on the manuscript. Brian Kauffman and Jeff Lee ran the Gent and Cane and the CSM models, respectively. Thanks also to William Kessler and Mike McPhaden for sharing the TOGA-TAO data with us. The National Center for Atmospheric Research is sponsored by the National Science Foundation.

REFERENCES

Ayotte, K. W., P. P. Sullivan, J. C. McWilliams, J. C. Wyngaard, C.-H. Moeng, A. Andren, S. C. Doney, B. Holtslag, W. G. Large and J. J. Tribbia, 1996: An evaluation of neutral and convective planetary boundary layer parameterizations relative to large eddy simulations. *Bound.-Layer Meteor.*, **79,** 131–175.

Berliand, M. E., and T. G. Berliand, 1952: Measurement of the effective radiation of the earth with varying cloud amounts. *Proc. Acad. Sci. USSR, Ser. Geophys.*, No. 1.

Bishop, J. K. B., and W. B. Rossow, 1991: Spatial and temporal variability of global surface solar irradiance. *J. Geophys. Res.*, **96,** 16 839–16 858.

Bryan, F. O., B. G. Kauffman, W. G. Large, and P. R. Gent, 1996: The NCAR CSM Flux Coupler. NCAR Tech. Note 424, 50 pp. [Available from NCAR, PO Box 3000, Boulder, CO 80305.]

Bryden, H. L., and E. C. Brady, 1989: Eddy momentum and heat fluxes and their effects on the circulation of the equatorial Pacific Ocean. *J. Mar. Res.*, **47,** 55–79.

Chen, D., L. M. Rothstein, and A. J. Busalacchi, 1994a: A hybrid vertical mixing scheme and its application to tropical ocean models. *J. Phys. Oceanogr.*, **24,** 2156–2179.

——, A. J. Busalacchi, and L. M. Rothstein, 1994b: The roles of vertical mixing, solar radiation, and wind stress in a model simulation of the sea surface temperature seasonal cycle in the tropical Pacific Ocean. *J. Geophys. Res.*, **99,** 20 345–20 359.

Deardorff, J. W., 1970: A numerical study of three-dimensional channel flow at large Reynolds numbers. *J. Fluid Mech.*, **41,** 453–480.

——, 1972: Numerical investigation of neutral and unstable planetary boundary layers. *J. Atmos. Sci.*, **29,** 91–115.

Fung, I. Y., D. E. Harrison, and A. A. Lacis, 1984: On the variability of the net longwave radiation at the ocean surface. *Rev. Geophys. Space Phys.*, **22,** 177–193.

Gent, P. R., 1991: The heat budget of the TOGA-COARE domain in an ocean model. *J. Geophys. Res.*, **96,** 3323–3330.

——, and M. A. Cane, 1989: A reduced gravity, primitive equation model of the upper equatorial ocean. *J. Comput. Phys.*, **81,** 444–480.

Gill, A. E., 1982: *Atmosphere–Ocean Dynamics*. Academic Press, 662 pp.

Gregg, M. C., H. Peters, J. C. Wesson, N. S. Oakey, and T. J. Shay, 1985: Intensive measurements of turbulence and shear in the equatorial undercurrent. *Nature*, **318,** 140–144.

Hurrell, J., J. J. Hack, B. A. Boville, D. Williamson, and J. T. Kiehl, 1998: The dynamical simulation of the NCAR CCM3. *J. Climate*, **11,** 1207–1236.

Jerlov, N. G., 1976: *Marine Optics*. Elsevier, 231 pp.

Kalnay, E., M. Kanamitsu, R. Kistler, W. Collins, D. Deaven, L. Gandin, M. Iredell, S. Saha, G. White, J. Woollen, Y. Zhu, M. Chelliah, W. Ebisuzai, W. Higgins, J. Janowiak, K. C. Mo, C. Ropelewski, A. Leetmaa, R. Reynolds, and R. Jenne, 1996: The NCEP/NCAR 40-Year Reanalysis Project. *Bull. Amer. Meteor. Soc.*, **77,** 437–471.

Kraus, E. B., and J. S. Turner, 1967: A one-dimensional model of the seasonal thermocline; II. The general theory and its consequences. *Tellus*, **19,** 98–105.

Large, W. G., J. C. McWilliams, and S. C. Doney, 1994: Oceanic vertical mixing: A review and a model with a nonlocal boundary layer parameterization. *Rev. Geophys.*, **32,** 363–403.

——, G. Danabasoglu, S. C. Doney, and J. C. McWilliams, 1997: Sensitivity to surface forcing and boundary layer mixing in a global ocean model: Annual-mean climatology. *J. Phys. Oceanogr.*, **27,** 2418–2447.

Ledwell, J. R., A. J. Wilson, and C. S. Low, 1993: Evidence for slow mixing across the pycnocline from an open-ocean tracer-release experiment. *Nature*, **364,** 701–703.

McPhaden, M. J., and M. E. McCarty, 1992: Mean seasonal cycles and interannual variations at 0,110W and 0,140W during 1980–1991. NOAA Tech. Memo. ERL PMEL-95, U.S. Department of Commerce, Washington, DC, 118 pp.

McWilliams, J. C., P. P. Sullivan, and C.-H. Moeng, 1997: Langmuir turbulence in the ocean. *J. Fluid Mech.*, **334,** 1–30.

Moeng, C.-H., and J. C. Wyngaard, 1984: Statistics of conservative scalars in the convective boundary layer. *J. Atmos. Sci.*, **41,** 3161–3169.

——, and ——, 1989: Evaluation of turbulent transport and dissipation closures in second-order modeling. *J. Atmos. Sci.*, **46,** 2311–2330.

Moum, J. N., and D. R. Caldwell, 1985: Local influences on the shear-flow turbulence in the equatorial ocean. *Science*, **230,** 315–316.

Pacanowski, R. C., and S. G. H. Philander, 1981: Parameterization of vertical mixing in numerical models of the tropical oceans. *J. Phys. Oceanogr.*, **11,** 1443–1451.

Paulson, C. A., and J. J. Simpson, 1977: Irradiance measurements in the upper ocean. *J. Phys. Oceanogr.*, **7,** 952–956.

Peters, H., M. C. Gregg, and J. M. Toole, 1988: On the parameterization of equatorial turbulence. *J. Geophys. Res.*, **93,** 1199–1218.

Philander, S. G. H., 1990: *El Nino, La Nina, and the Southern Oscillation*. Academic Press, 289 pp.

——, W. J. Hurlin, and A. D. Siegel, 1987. Simulation of the seasonal cycle of the tropical Pacific Ocean. *J. Phys. Oceanogr.*, **17,** 1986–2002.

Price, J. F., R. A. Weller, and R. Pinkel, 1986: Diurnal cycling: Observations and models of the upper ocean response to diurnal heating, cooling and wind mixing. *J. Geophys. Res.*, **91,** 8411–8427.

Reynolds, R. W., and T. M. Smith, 1994: Improved global sea temperature analyses using optimum interpolation. *J. Climate*, **7,** 929–948.

Rossow, W. B., and R. A. Schiffer, 1991: ISCCP cloud data products. *Bull. Amer. Meteor. Soc.*, **72,** 2–20.

Seager, R., S. E. Zebiak, and M. A. Cane, 1988: A model of the tropical Pacific sea surface temperature climatology. *J. Geophys. Res.*, **93,** 1265–1280.

Skyllingstad, E. D., and D. W. Denbo, 1995: An ocean large eddy simulation of Langmuir circulations and convection in the surface mixed layer. *J. Geophys. Res.*, **100,** 8501–8522.

——, W. D. Smyth, J. N. Moum, and H. Wijesekera, 1999: Turbulent dissipation during a westerly wind burst: A comparison of large eddy simulation results and microstructure measurements. *J. Phys. Oceanogr.*, **29,** 5–28.

Wang, D., W. G. Large, and J. C. McWilliams, 1996: Diurnal cycling, eddy viscosity and horizontal rotation effects in equatorial ocean boundary layers. *J. Geophys. Res.*, **101,** 3649–3662.

——, J. C. McWilliams, and W. G. Large, 1998: Large eddy simulation of the diurnal cycle of deep equatorial turbulence. *J. Phys. Oceanogr.*, **28,** 129–148.

Wyngaard, J. C., 1982: Lectures on the planetary boundary layer. *Mesoscale Meteorology—Theories, Observations and Models*, D. K. Lilly and T. Gal-Chen, Eds., NATO ASI Series, D. Reidel. 781 pp.

——, and R. A. Brost, 1984: Top-down and bottom-up diffusion in the convective boundary layer. *J. Atmos. Sci.*, **41,** 102–112.